IJRCS

International Journal of Robotics and Control Systems
Vol. 2, No. 2, 2022, pp. 332-356
ISSN 2775-2658
http://pubs2.ascee.org/index.php/ijrcs

ASCEE

Sliding Mode Controller Based on the Sliding Mode Observer for a QBall 2+ Quadcopter with Experimental Validation

Ayoub Daadi [a,1], Houssam Boulebtinai [a,2], Saddam Hocine Derrouaoui [a,3,*], Fares Boudjema [a,4]

[a] Ecole Supérieure Ali Chabati, Algires, Algeria
[1] daadiayoub2022@gmail.com; [2] HoussamBoulebtinai@gmail.com; [3] derrouaouish@gmail.com;
[4] fboudjema@yahoo.fr
[*] Corresponding Author

ARTICLE INFO

Article History
Received April 22, 2022
Revised May 15, 2022
Accepted May 27, 2022

Keywords
QBall 2+ quadcopter;
PID controller;
Sliding Mode Observer;
Sliding Mode Control;
Flight tests

ABSTRACT

This paper studies a particular Unmanned Aerial Vehicle (UAV), called QBall 2+ quadcopter. This vehicle is a complex system, non-linear, strongly coupled, and under-actuated. First, a non-linear model was developed to represent the dynamics of the studied drone. Once the latter is established, the linear model was used to obtain the best gains of the Proportional Integral Derivative (PID) controller. This controller was applied after on the non-linear model of the UAV. Moreover, a Sliding Mode Controller (SMC) based on Sliding Mode Observer (SMO) was designed for retrieving the system unknown variables. Through these latter, the QBall 2+ was controlled, taking into account the observer errors. The first contribution in this work is to implement the PID regulator on the QBall 2+ flight controller to validate the results obtained by simulation. Secondly, due to the limitations of the Flex 3 cameras, especially when the drone is outside their working environment, the sliding mode observer was implemented to replace the cameras in order to measure the states of the system considered in this work. Simulation results of the different applied controllers were displayed to evaluate their effectiveness.

1. Introduction

Recently, in the field of flying robots, the use of quadrotors has drastically increased. They have many advantages compared to the fixed-wing drones in terms of maneuverability, structure and versatility. Moreover, they have a simple mechanical design, a small size and a low cost [1, 2, 3, 4, 5, 6, 7]. Quadrotors are widely exploited in military and civilian missions such as, search and rescue, mapping, protection of sensitive points, and infrastructure inspection [8, 9, 10, 11, 12]. The QBall 2 quadcopter is an innovative platform intended for scientific research to fly indoor using Optitrack Flex-3 cameras [13]. It has a strongly coupled dynamics and an external protective cage [13, 14, 15, 16, 17]. It was built by Quanser, a Canadian robot manufacturing company. It has an open architecture design that allows operators to test a variety of controllers ranging from basic flight dynamics stabilizers to advanced multi-vehicle path planning and navigation algorithms. The drone has an on-board data acquisition system, an on-board computer and a suite of sensors. The Qball 2+ is an innovative rotary wing vehicle platform suitable for a wide variety of research applications on UAVs. However, it has a working environment limitation by the field of view of the Flex 3 cameras, which are sensitive to light resources and ground reflection. It is designed with an outer protective cage. In the real prototype, the cage gives the QBall 2+ a decisive advantage over other vehicles that would cause significant damage

in the event of contact between the vehicle and an obstacle, or in the event of a failure [13].

The researchers in paper [18], have performed an Extended Kalman Filter (EKF), this non-linear observer was exploited to control the QBall 2 drone. In addition, they have also applied a Linear Quadratic Regulator (LQR) on the same system to evaluate its performance. Moreover, the obtained results of the designed observer are satisfactory in the presence of model uncertainty. The authors in work [19], have designed an optimal PID controller with a Kalman filter. The latter is based on the time integral taking into account the errors of the system. However, they did not consider the different faults of the drone. In the same context, an Observer based on Sliding Mode Control (OSMC) has been considered in [20, 21, 22], to overcome the practical limitations of rotational and translation speed. A nonlinear PID controller with gains tuning has been implemented to follow the desired 3D trajectory of the QBall 2 quadrotor [23]. In addition, the experimental tests were carried out, where the quadrotor is subjected to external disturbances (gust of wind) in flight. An optimal fault tolerant controller was applied to stabilize the QBall 2 drone [24]. This approach is based mainly on a Finite Time Sliding Mode Observer (FTSMO), which estimates the completeness from outputs and allows to identify the disturbances type. In addition, the proposed strategy has proven its robustness under the influence of external disturbances and uncertainties. In reference [25], the researchers have introduced a new Lyapunov-based trajectory tracking approach to control and stabilize a quadrotor UAV. Furthermore, they have diagnosed an actuator failure using an intelligent output estimator. In article [26], two control algorithms have been applied on a quadrotor drone. The first one is designed to detect and diagnose actuator faults, where the second one works online after detecting the actuator faults. Kose et al. [27], have developed a dynamic model and Matlab simulation for the QBall 2. The developed model was validated through various flight scenarios. More recently, Wang et al. [28], have designed and applied an adaptive fault tolerant approach to control a small quadcopter. This approach was tested against actuator faults as well as unknown system parameters. However, the different external disturbances were not studied in this work.

The first contribution in this work is to implement the PID regulator on the QBall 2+ flight controller to validate the results obtained by simulation. To achieve this goal, the various ”Optitrack Flex-3” cameras must be calibrated and tested to locate the position of the quadcopter. Secondly, due to the limitations of the Flex 3 cameras, especially when the drone is outside their working environment, the sliding mode observer was implemented to replace the cameras in order to measure the states of the system considered in this work.

The paper is structured as follows: In Section 1, a mathematical model that represents the dynamic behavior of the QBall 2 was developed. Section 2 explains the design steps of the different control techniques. Simulation results were displayed in Section 3. Section 4 is devoted to validate the PID controller through some experimental tests. Section 5 is intended for conclusion and future works.

2. Modeling of QBall 2+

The following assumptions are taken into account for the dynamic model of QBall 2+ [28]:

- The structure of the QBall 2+ is assumed to be rigid and symmetrical, which means that the inertia matrix is diagonal.
- The propellers are supposed to be rigid in order to neglect the effect of their deformation during the rotation.
- The inertia matrix $J \in \mathbb{R}^{3\times3}$ is assumed to be constant.
- The origin of the body frame is supposed to coincide with the center of gravity (see Fig. 1).

With aim to simplify the understanding of the multitude of variables and terms of this work, the notation Table is given as follows (see Table 1).

Table 1. Table of notation.

Symbols	Notation
$[\text{x y z}]^T$	Position vector
$\dot{\chi} = [\dot{x}\ \dot{y}\ \dot{z}]^T$	Translation speeds vector.
$[\ddot{x}\ \ddot{y}\ \ddot{z}]^T$	Translation accelerations vector.
$[\theta\ \phi\ \psi]^T$	Euler angles vector.
$\Omega = [\text{p q r}]^T$	Rotation speed vector.
$\dot{\Omega} = [\dot{p}\ \dot{q}\ \dot{r}]^T$	Vector of angular accelerations.
$V = [u\ \upsilon\ \omega]^T$	Vector of linear velocities in the body frame.
J	Matrix of angular moments.
I_{xx}	Moment of inertia of the quadcopter along the x axis (Roll axes).
I_{yy}	Moment of inertia of the quadcopter along the y axis (Pitch axes).
I_{yz}	Moment of inertia of the quadcopter along the z axis (Yaw axes).
J_r	Represents the inertia matrix of each rotor.
J_{rx}	Inertia of the rotor along the x axis.
J_{ry}	Inertia of the rotor along the y axis.
J_{rz}	Inertia of the rotor along the z axis.
M	Mass of QBall 2+.
P	Weight of the QBall 2+.
R_0	Terrestrial landmark.
R_1	Landmark linked to the body of the quadcopter.
R_p	Crossing matrix of R_0 to R_1.
$F_{g_{R_0}}$	Force of gravity.
F_i	Thrust generated by each propeller.
$F_{P_{R_1}}$	Lift created by the propellers in body frame.
D_{R_1}	Drag Force.
K_d	Drag coefficient.
τ_{R_I}	Torques applied to the quadcopter.
L	Distance between the center of gravity and the axis of rotation of the rotor.
τ_i	Torque generated by each motor.
τ_{gyr}	Gyroscopic moment.
K_υ	Voltage transformation constant at the input of each motor to angular velocity.
υ	Battery output voltage.
τ_f	Friction torque.
k_f	Coefficient of friction.
$U = [U_1\ U_2\ U_3\ U_4]^T$	Control vector.
u_i	Input Pulse Width Modulation (PWM) of actuator i.
V_i	Lyapunov's function.

2.1. Translation Dynamics

Using Newton-Euler's law, which is the sum of all external forces acting on a rigid body and equal the modulus of its mass per acceleration as following

$$\begin{aligned} F_{R_0} &= M\frac{d}{dt}(V_{R_0}) \\ F_{R_1} &= M\dot{V}_{R_1} + M(\Omega \wedge V_{R_1}) \end{aligned} \tag{1}$$

where

$$\Omega \wedge V_{R_1} = \begin{bmatrix} qw - rv \\ ru - pw \\ pv - qu \end{bmatrix} \tag{2}$$

where $(\Omega \wedge V_{R_1})$ is called the Coriolis term indicating the coriolis effects, and M is the quadrotor mass.

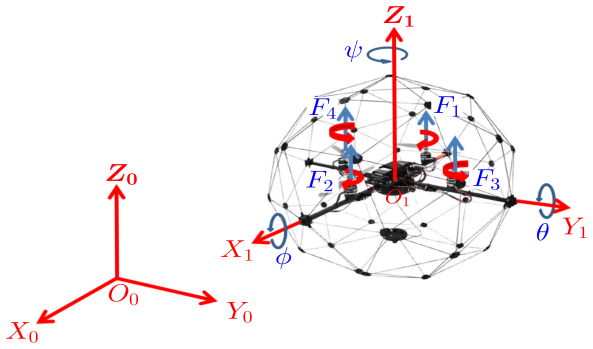

Fig. 1. Frames used to describe the movement of the Qball 2+.

The main forces applied on QBall 2+ are defined as

- **Force of gravity**

The force of gravity $F_{g_{R_0}} = [\,0\;0\;\text{-Mg}\,]^T$ in the fixed frame is along the Z axis (yaw axis), its expression in the mobile frame R_1 is giving as follows

$$F_{g_{R_1}} = R_p^T F_{g_{R_0}} = R_p^T \begin{bmatrix} 0 \\ 0 \\ -Mg \end{bmatrix} = \begin{bmatrix} Mg\sin(\theta) \\ -Mg\sin(\phi)\cos(\theta) \\ -Mg\cos(\phi)\cos(\theta) \end{bmatrix} \tag{3}$$

with R_p^T is the passage matrix from the fixed frame to the body frame, and

$$R_p = \begin{bmatrix} C(\psi)C(\theta) & C(\psi)S(\theta)S(\phi) - S(\psi)C(\phi) & C(\psi)S(\theta)C(\phi) + S(\psi)S(\phi) \\ S(\psi)C(\theta) & S(\psi)S(\theta)S(\phi) + C(\psi)C(\phi) & S(\psi)S(\theta)C(\phi) - C(\psi)S(\phi) \\ -S(\theta) & C(\theta)S(\phi) & C(\theta)C(\phi) \end{bmatrix} \tag{4}$$

with

$C(x) = \cos(\text{x})$ and $S(x) = \sin(x)$.

- **Force of thrust**

It is a resultant obtained by the rotation of each rotor, it is parallel to the Z axis expressed in the body frame R_1. The thrust generated by each propeller is modeled using a first order function [13]. Its model is different to the model of the conventional quadrotors, where it is given by

$$F_i = K\frac{w}{s+w}u_i, \qquad i = 1, 2, 3, 4. \tag{5}$$

with K is a positive gain and ω is the actuator bandwidth.

- **Force of drag**

  It's expressed in the body frame as [29, 30]

$$D_{R_1} = \quad -K_d\dot{\chi} \tag{6}$$

  with K_d represents the drag coefficient.

  According to Equations (5) and (6), we get the various forces expressed in the body frame as following

$$F_{T_{R_1}} = F_{g_{R_1}} + F_P + D_{R_1} \tag{7}$$

  Therefore, Equations (1) and (7) become

$$\begin{cases} M\dot{u} + M(qw - rv) = -Mg\sin(\theta) - K_x\dot{x} \\ M\dot{v} + M(ru - pw) = Mg\sin(\phi)\cos(\theta) - K_y\dot{y} \\ M\dot{w} + M(pv - qu) = Mg\cos(\theta)\cos(\psi) - K_z\dot{z} + F_{P_{R_1}} \end{cases} \tag{8}$$

2.2. Rotation Dynamics

Using Newton's second law, which is the sum of the external moments equal to the temporal variation of the angular momentum as follows

$$\begin{aligned} \tau_{R_0} &= J\tfrac{d}{dt}(\Omega_{R_0}) \\ \tau_{R_1} &= J\dot{\Omega} + \Omega \wedge J\Omega \end{aligned} \tag{9}$$

where τ_{R_0} and τ_{R_1} are the moments applied on the quadrotor expressed in the fixed and mobile frames respectively.

The different moments (roll, pitch, yaw), which cause the rotation of the QBall 2 along the three axes (see Fig. 2) are given as follows

$$\begin{cases} \tau_{\theta_{R_1}} = L(F_1 - F_2) \\ \tau_{\phi_{R_1}} = L(F_3 - F_4) \\ \tau_{\psi_{R_1}} = \tau_1 + \tau_2 - \tau_3 - \tau_4 \end{cases} \tag{10}$$

where L represents the distance between the center of gravity and the axis of rotation of the rotor, τ_i is the torque generated by each rotor, it is assumed to have the following relation with respect to the PWM input as

$$\tau_i = K_y u_i, \qquad i = 1, 2, 3, 4. \tag{11}$$

where K_y is a positive gain.

- **Gyroscopic moment**

  It is general expression is given by:

$$\tau_{gyr} = \begin{bmatrix} (u_3 + u_4 - u_1 - u_2)J_{rz}qK_v\upsilon \\ (u_1 + u_2 - u_3 - u_4)J_{rz}pK_v\upsilon \\ 0 \end{bmatrix} \tag{12}$$

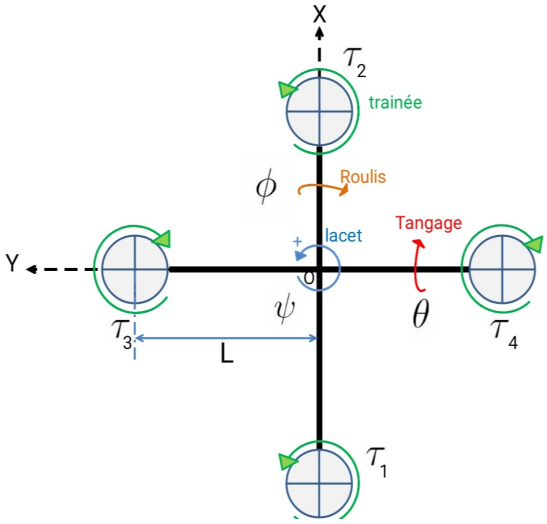

Fig. 2. Schematic representation of QBall 2+.

- **Friction torque**

It's the resultant of the aerodynamic friction couples. It is modeled as

$$\tau_f = k_f \Omega^2 \tag{13}$$

with

$$k_f = \begin{bmatrix} k_{fx} & 0 & 0 \\ 0 & k_{fy} & 0 \\ 0 & 0 & k_{fz} \end{bmatrix} \tag{14}$$

Equation (9) becomes

$$\begin{cases} J_{xx}\dot{p} + qr(J_{zz} - J_{yy}) = L(F_3 - F_4) - J_{rz}qu_g - k_{fx}p^2 \\ J_{yy}\dot{q} + pr(J_{xx} - J_{zz}) = L(F_1 - F_2) + J_{rz}pu_g - k_{fy}q^2 \\ J_{zz}\dot{r} + pq(J_{yy} - J_{xx}) = \tau_1 + \tau_2 - \tau_3 - \tau_4 - k_{fz}r^2 \end{cases} \tag{15}$$

with $u_g = (u_1 + u_2 - u_3 - u_4)K_v v$.

Due to the weak orientations of QBall 2+, the relation which connects the angular speeds expressed in reference R_1 and the derivatives of the angles of Euler expressed in reference R_0 is given by

$$(\dot{\phi}, \dot{\theta}, \dot{\psi}) \approx (p, q, r) \tag{16}$$

From Equations (8), (15) and (16), the dynamics model of QBall 2+ in the fixed frame is represented by the following state equations

$$\begin{cases} \ddot{x} = \frac{1}{M}F_{P_{R_1}}(C(\psi)S(\theta)C(\phi) + S(\psi)S(\phi)) - \frac{K_x}{M}\dot{x} \\ \ddot{y} = \frac{1}{M}F_{P_{R_1}}(S(\psi)S(\theta)C(\phi) - C(\psi)S(\phi)) - \frac{K_y}{M}\dot{y} \\ \ddot{z} = \frac{1}{M}F_{P_{R_1}}(C(\theta)C(\phi)) - \frac{K_z}{M}\dot{z} - g \\ \ddot{\phi} = \frac{L(F_3 - F_4)}{J_{xx}} - \frac{J_{rz}qu_g}{J_{xx}} - \frac{\dot{\theta}\dot{\psi}(J_{zz} - J_{yy})}{J_{xx}} - \frac{k_{fx}}{J_{xx}}p^2 \\ \ddot{\theta} = \frac{L(F_1 - F_2)}{J_{yy}} + \frac{J_{rz}pu_g}{J_{yy}} - \frac{\dot{\phi}\dot{\psi}(J_{xx} - J_{zz})}{J_{yy}} - \frac{k_{fy}}{J_{yy}}q^2 \\ \ddot{\psi} = \frac{\tau_1 + \tau_2 - \tau_3 - \tau_4}{J_{zz}} - \frac{\dot{\phi}\dot{\theta}(J_{yy} - J_{xx})}{J_{zz}} - \frac{k_{fz}}{J_{zz}}r^2 \end{cases} \tag{17}$$

3. Control of QBall 2+

3.1. Linear Control Model

In the almost stationary state, it is shown that the total thrust is approximately equal to the weight, i.e $F_{P_{R_1}} \approx Mg$ [31]. Due to the small amplitude movements of QBall 2+, it's assumed that

$$\cos(\phi) = 1; \cos(\theta) = 1; \cos(\psi) = 1 \;\; and \;\; \sin(\phi) = \phi; \sin(\theta) = \theta; \sin(\psi) = \psi \tag{18}$$

Then, the dynamics of QBall 2 expressed by Equation (17) can be simplified as follows:

$$\begin{cases} \ddot{x} = g\theta \\ \ddot{y} = -g\phi \\ \ddot{z} = \frac{1}{M} F_{P_{R_1}} - g \\ \ddot{\phi} = \frac{L(F_3 - F_4)}{J_{xx}} \\ \ddot{\theta} = \frac{L(F_1 - F_2)}{J_{yy}} \\ \ddot{\psi} = \frac{\tau_1 + \tau_2 - \tau_3 - \tau_4}{J_{zz}} \end{cases} \tag{19}$$

3.2. Nonlinear Control Model

For the nonlinear control model, the state equations are used as

$$\begin{cases} \dot{x}_1 = x_2 \\ \dot{x}_2 = a_1 x_4 x_6 + a_2 x_2^2 + a_3 x_4 u_g + b_1 U_2 \\ \dot{x}_3 = x_4 \\ \dot{x}_4 = a_4 x_2 x_6 + a_5 x_4^2 + a_6 x_2 u_g + b_2 U_3 \\ \dot{x}_5 = x_6 \\ \dot{x}_6 = a_7 x_2 x_4 + a_8 x_6^2 + b_3 U_4 \\ \dot{x}_7 = x_8 \\ \dot{x}_8 = a_9 x_8 + \frac{U_x}{M} U_1 \\ \dot{x}_9 = x_{10} \\ \dot{x}_{10} = a_{10} x_{10} + \frac{u_y}{M} U_1 \\ \dot{x}_{11} = x_{12} \\ \dot{x}_{12} = a_{11} x_{12} + \frac{1}{M} U_1 c(x_1) c(x_3)) - g \end{cases} \tag{20}$$

with

$a_1 = -\frac{(J_{zz} - J_{yy})}{J_{xx}}$, $a_2 = -\frac{k_{fx}}{J_{xx}}$, $a_3 = -\frac{J_{rz}}{J_{xx}}$, $b_1 = \frac{L}{J_{xx}}$

$a_4 = -\frac{(J_{xx} - J_{zz})}{J_{yy}}$, $a_5 = -\frac{k_{fy}}{J_{yy}}$, $a_6 = \frac{J_{rz}}{J_{yy}}$, $b_2 = \frac{L}{J_{yy}}$

$a_7 = -\frac{(J_{yy}-J_{xx})}{J_{zz}}$, $a_8 = -\frac{k_{fz}}{J_{zz}}$, $b_3 = \frac{1}{J_{zz}}$

$a_9 = -\frac{K_x}{M}$,$a_{10} = -\frac{K_y}{M}$,$a_{11} = -\frac{K_z}{M}$

$U_X = C(x_1)S(x_3)C(x_5) + S(x_1)S(x_5)$

$U_y = C(x_1)S(x_3)S(x_5) - S(x_1)C(x_5)$

The control vector is expressed by a thrust force and moments as

$$U = [U_1 \;\; U_2 \;\; U_3 \;\; U_4]^T$$

with

$$\begin{bmatrix} U_1 \\ U_2 \\ U_3 \\ U_4 \end{bmatrix} = \begin{bmatrix} k & k & k & k \\ 0 & 0 & k & -k \\ k & -k & 0 & 0 \\ k_y & k_y & -k_y & -k_y \end{bmatrix} \begin{bmatrix} u_1 \\ u_2 \\ u_3 \\ u_4 \end{bmatrix} \tag{21}$$

The choice of state vector is given as follows

$$X = \left\{ \begin{array}{cccccccccccc} \phi & \dot{\phi} & \theta & \dot{\theta} & \psi & \dot{\psi} & x & \dot{x} & y & \dot{y} & z & \dot{z} \end{array} \right\} \tag{22}$$

The system outputs are given as

$$Y = [\phi \;\; \theta \;\; \psi \;\; x \;\; y \;\; z]^T$$

3.3. PID Controller Design

Here, the PID controller based on the linear model presented by (19) is designed. This control law will be applied after to the nonlinear control model presented by (20).

The PID control laws are given as

$$U_1 = K_{pz}e_z + K_{iz}\int_0^{+\infty} e_z + K_{dz}\frac{de_z}{dt} \tag{23}$$

$$U_2 = K_{p\phi}e_\phi + K_{i\phi}\int_0^{+\infty} e_\phi + K_{d\phi}\frac{de_\phi}{dt} \tag{24}$$

$$U_3 = K_{p\theta}e_\theta + K_{i\theta}\int_0^{+\infty} e_\theta + K_{d\theta}\frac{de_\theta}{dt} \tag{25}$$

$$U_4 = K_{p\psi}e_\psi + K_{i\psi}\int_0^{+\infty} e_\psi + K_{d\psi}\frac{de_\psi}{dt} \tag{26}$$

After choosing the altitude and attitude regulators, a position controller is developed. The PID controllers are used to calculate the desired positions [32], and the desired roll ϕ_d and pitch θ_d angles, which are given by

$$\begin{cases} \theta_d = K_{px} * e_x + K_{ix} * \int_0^{+\infty} e_x + K_{dx} * \frac{de_x}{dt} \\ \\ \phi_d = K_{py} * e_y + K_{iy} * \int_0^{+\infty} e_y + K_{dy} * \frac{de_y}{dt} \end{cases} \tag{27}$$

with $e_z = z_d - z$, $e_\phi = \phi_d - \phi$, $e_\theta = \theta_d - \theta$, $e_\psi = \psi_d - \psi$, $e_x = x_d - x$, $e_y = y_d - y$, and K_P, K_i and K_d are respectively proportional, integral and derivative gains.

3.4. Sliding Mode Observer (SMO) Design

3.4.1 Sliding Mode Observer State Model

In this subsection, a nonlinear sliding mode observer is designed. The latter will be tested against uncertain system parameters. The observer state model is given by

$$\hat{\Sigma}: \begin{cases} \dot{\hat{x}}_1 = \hat{x}_2 + \Lambda_1(z_1) \\ \dot{\hat{x}}_2 = a_1\hat{x}_4\hat{x}_6 + a_2\hat{x}_2^2 + a_3\hat{x}_4 u_g + b_1 U_2 + \Lambda_2(z_2) \\ \dot{\hat{x}}_3 = \hat{x}_4 + \Lambda_3(z_3) \\ \dot{\hat{x}}_4 = a_4\hat{x}_2\hat{x}_6 + a_5\hat{x}_4^2 + a_6\hat{x}_2 u_g + b_2 U_3 + \Lambda_4(z_4) \\ \dot{\hat{x}}_5 = \hat{x}_6 + \Lambda_5(z_5) \\ \dot{\hat{x}}_6 = a_7\hat{x}_2\hat{x}_4 + a_8\hat{x}_6^2 + b_3 U_4 + \Lambda_6(z_6) \\ \dot{\hat{x}}_7 = \hat{x}_8 + \Lambda_7(z_7) \\ \dot{\hat{x}}_8 = a_9\hat{x_8} + \frac{\hat{U_x}}{M} U_1 + \Lambda_8(z_8) \\ \dot{\hat{x}}_9 = \hat{x}_{10} + \Lambda_9(z_9) \\ \dot{\hat{x}}_{10} = a_{10}\hat{x}_{10} + \frac{\hat{U_y}}{M} U_1 + \Lambda_{10}(z_{10}) \\ \dot{\hat{x}}_{11} = \hat{x}_{12} + \Lambda_{11}(z_{11}) \\ \dot{\hat{x}}_{12} = a_{11}\hat{x}_{12} + \frac{1}{M} U_1 (c(\hat{x}_1)c(\hat{x}_3)) - g + \Lambda_{12}(z_{12}) \end{cases} \tag{28}$$

where the dynamic of the observer errors is expressed as follows

$$\begin{cases} \dot{z}_1 = z_2 - \Lambda_1 \\ \dot{z}_2 = a_1\Delta_{x_4x_6} + a_2\Delta_{x_2^2} + a_3\Delta_{x_4}u_g - \Lambda_2 \\ \dot{z}_3 = z_4 - \Lambda_3 \\ \dot{z}_4 = a_4\Delta_{x_2x_6} + a_5\Delta_{x_4^2} + a_6\Delta_{x_2}u_g - \Lambda_4 \\ \dot{z}_5 = z_6 - \Lambda_5 \\ \dot{z}_6 = a_7\Delta_{x_2x_4} + a_8\Delta_{x_6^2} - \Lambda_6 \\ \dot{z}_7 = z_8 - \Lambda_7 \\ \dot{z}_8 = a_9 z_8 + \frac{1}{M}\Delta_{U_x} U_1 - \Lambda_8 \\ \dot{z}_9 = z_{10} - \Lambda_9 \\ \dot{z}_{10} = a_{10} z_{10} + \frac{1}{M}\Delta_{U_y} U_1 - \Lambda_{10} \\ \dot{z}_{11} = z_{12} - \Lambda_{11} \\ \dot{z}_{12} = a_{11} z_{12} + \frac{1}{M} U_1 \Delta_{(c(x_1)c(x_3))} - \Lambda_{12} \end{cases} \tag{29}$$

with

$$\begin{cases} \Delta_{x_ix_j} = x_ix_j - \hat{x}_i\hat{x}_j & \Delta_{(c(x_1)c(x_3))} = (c(x_1)c(x_3)) - (c(\hat{x}_1)c(\hat{x}_3)) \\ \Delta_{x_i^2} = x_i^2 - \hat{x}_i^2 & \Delta_{U_x} = U_x - U_{\hat{x}} \\ \Delta_{x_i} = x_i - \hat{x}_i & \Delta_{U_y} = U_y - U_{\hat{y}} \end{cases} \tag{30}$$

and

$$\begin{cases} z_i = y_i - \hat{y}_i & if \quad i \ \ odd. \\ z_i = x_i - \hat{x}_i & if \quad i \ \ pair. \end{cases} \tag{31}$$

with

$$\Lambda_i(z_i) = K_i sign(x_i - \hat{x}_i)$$

3.4.2 Observer Design Assumptions

With the aim to design the sliding mode observer, we must define the measured states and the missing states. The measurements of the optitrack cameras are:

$$\begin{cases} \phi = x_1 & \dot{\phi} = x_2 & x = x_7 \\ \theta = x_3 & \dot{\theta} = x_4 & y = x_9 \\ \psi = x_5 & \dot{\psi} = x_6 & z = x_{11} \end{cases} \tag{32}$$

Nevertheless, the unmeasured states are given as

$$\begin{cases} \dot{x} = x_8 \\ \dot{y} = x_{10} \\ \dot{z} = x_{12} \end{cases} \tag{33}$$

3.4.3 Observer Stability Analysis

In order to study the stability and the convergence of the observer, it's necessary to choose the candidate Lyapunov function, which is a function of the error and then the stability has to be proved. The errors must converge to zero i.e. the estimated states must converge to the actual states after the following steps.

- **Step 1**: Considering the dynamics of the error of the first observer as

$$\dot{z}_1 = z_2 - K_1 sign(z_1) \tag{34}$$

The choose of the Lyapunov function is giving as following

$$V_1 = \frac{1}{2} z_1^2 \tag{35}$$

Its derivative is given as

$$\dot{V}_1 = z_1 \dot{z}_1 = z_1(z_2 - K_1 sign(z_1)) \tag{36}$$

So that $\hat{x}_1 \to x_1$ it is necessary that $\dot{V}_1 < 0$. For that, the K_1 is chosen as

$$K_1 > |z_2|_{max} \tag{37}$$

Then, the error $z_1 \to 0$ after a finite time t_1, which gives

$$z_2 = K_1 sign(z_1) \tag{38}$$

After that, x_2 becomes

$$x_2 = \hat{x}_2 + K_1 sign(z_1) \tag{39}$$

- **Step 2**: In this step, z_2 converges towards zero.

  To stay on the surface $z_2 = 0$, it must be $K_1 > |z_2|_{max}$, but this is verified if z_2 decreases after t_1.

  The dynamics of error z_2 becomes

$$\dot{z}_2 = a_1\Delta_{x_4x_6} + a_2\Delta_{x_2^2} + a_3\Delta_{x_4}u_g - K_2 sign(z_2)$$

  Then, the Lyapunov function is taken as

$$V_2 = \tfrac{1}{2}z_1^2 + \tfrac{1}{2}z_2^2$$

  Its derivative is

$$\dot{V}_2 = z_1\dot{z}_1 + z_2\dot{z}_2 = z_2(a_1\Delta_{x_4x_6} + a_2\Delta_{x_2^2} + a_3\Delta_{x_4}u_g - K_2 sign(z_2))$$

  To get $\dot{V}_2 < 0$, it's necessary to choose

$$K_2 > |a_1\Delta_{x_4x_6} + a_2\Delta_{x_2^2} + a_3\Delta_{x_4}u_g|_{max}$$

  Therefore, $z_2 \to 0$ after a finite time t_2.

  The steps 3, 5, 7, 9, and 11 are identical to step 1, where the obtained results are:

- **Step 3**: $K_3 > |z_4|_{max}$, therefore $z_3 \to 0$ after a t_3 finished, and $x_4 = \hat{x}_4$.

- **Step 5**: $K_5 > |z_6|_{max}$, therefore $z_6 \to 0$ after a t_5 finished, and $x_6 = \hat{x}_6$.

- **Step 7**: $K_7 > |z_8|_{max}$, therefore $z_7 \to 0$ after a t_7 finished, and $x_8 = \hat{x}_8$.

- **Step 9**: $K_9 > |z_{10}|_{max}$, therefore $z_9 \to 0$ after a t_9 finished, and $x_{10} = \hat{x}_{10}$.

- **Step 11**: $K_{11} > |z_{12}|_{max}$, therefore $z_{11} \to 0$ after a t_{11} finished, and $x_{12} = \hat{x}_{12}$.

  Also for the steps 4, 6, 8, 10, and 12 will be identical to step 2.

- **Step 4**: The dynamics of error z_4 will be:

$$\dot{z}_4 = a_4\Delta_{x_2x_6} + a_5\Delta_{x_4^2} - K_4 sign(z_4)$$

  Involved

$$K_4 > |a_4\Delta_{x_2x_6} + a_5\Delta_{x_4^2}|_{max}$$

  To ensure the convergence of $z_4 \to 0$ after a finite time t_4.

- **Step 6**: The dynamics of error z_6 will be

$$\dot{z}_6 = a_8 \Delta_{x_6^2} - K_6 sign(z_6)$$

Involved

$$K_6 > |a_8 \Delta_{x_6^2}|_{max}$$

To ensure the convergence of $z_6 \to 0$ after a finite time t_6.

- **Step 8**: The dynamics of error z_8 will be

$$\dot{z}_8 = -K_8 sign(z_8)$$

$(U_x - U_{\hat{x}}) = 0$ because $U_x \; and \; U_{\hat{x}}$ are modeled according to $(x_1, x_3, x_5) \; and \; (\hat{x}_1, \hat{x}_3, \hat{x}_5)$ respectively.
Here, the choice of K_8 is given as

$$K_8 > 0$$

To ensure the convergence of $z_8 \to 0$ after a finite time t_8.

- **Step 10**: The dynamics of error z_{10} will be

$$\dot{z}_8 = -K_{10} sign(z_{10})$$

$(U_y - U_{\hat{y}}) = 0$ because $U_y \; and \; U_{\hat{y}}$ are modeled according to $(x_1, x_3, x_5) \; and \; (\hat{x}_1, \hat{x}_3, \hat{x}_5)$ respectively.
The choice of K_{10} is given as

$$K_{10} > 0$$

To ensure the convergence of $z_{10} \to 0$ after a finite time t_{10}.

- **Step 12**: The dynamics of error z_{12} will be

$$\dot{z}_{12} = -K_{12} sign(z_{12})$$

$\Delta_{(c(x_1)c(x_3))} = 0$ are modelled according to (x_1, x_3) and $(\hat{x}_1, \hat{x}_3)$.
In this step, the choice of K_{12} is given as

$$K_{12} > 0$$

To ensure the convergence of $z_{12} \to 0$ after a finite time t_{12}.

3.5. Sliding Mode Control Law Design

The choice of the sliding surface is given by a general form as

$$S = \dot{Z}_i + \alpha_i Z_i, \qquad Z_i = x_{id} - x_i \tag{40}$$

Its derivative is obtained as

$$\dot{S}_i = -k_i sign(S_i) = \ddot{Z}_i + \alpha_i \dot{Z}_i \tag{41}$$

The control law U_1 is developed as follows.

We assume that

$$z_{11} = z_d - x_{11} \Longrightarrow \dot{z}_{11} = \dot{z}_d - \dot{x}_{11} = \dot{z}_d - x_{12} \tag{42}$$

We replace x_{12} by $\hat{x}_{12} + e_{12}$

$$\ddot{z}_{11} = \ddot{z}_d - \dot{x}_{12} = \ddot{z}_d - (\dot{\hat{x}}_{12} + \dot{e}_{12}) \tag{43}$$

Therefore

$$\ddot{z}_{11} = \ddot{z}_d - e_{12} - g - k_{12} sat(e_{11}) - \frac{C(x_1)C(x_2)}{M} U_1 \tag{44}$$

Now, we suppose that e_{12} and $\dot{e}_{12}$ are bounded which gives:

$$\begin{cases} e_{12} \leq \mid e_{12} \mid_{max} = \beta_{12} e \\ \dot{e}_{12} \leq \mid \dot{e}_{12} \mid_{max} = \dot{\beta}_{12}. \end{cases} \tag{45}$$

Thus

$$\dot{S}_{11} = g + \ddot{z}_d - \dot{e}_{12} - k_{12} sat(e_{11}) + \alpha_{11}(\dot{z}_d - \dot{\hat{x}}_{12} - e_{12}) - \frac{C(x_1)C(x_2)}{M} U_1 - a_{11}\hat{x}_{12} = -k_{11} sign(S_{11}) \tag{46}$$

We use the upper terms, we find

$$U_1 = \frac{M}{C(x_1)C(x_2)} (k_{11} sign(S_{11}) + \alpha_{11}(\dot{z}_d - \hat{x}_{12} - \beta_{12}) + g + \ddot{z}_d - a_{11}\hat{x}_{12} - \dot{\beta}_{12} - K_{12} sat(e_{11})) \tag{47}$$

Adopting the same steps of development, we obtain the others controllers represented by the system of equations as

$$\begin{cases} U_2 = \frac{1}{b_1}[k_1 sign(S_\phi) + \ddot{\phi}_d + \alpha_1 (\dot{\phi}_d - x_2) - a_1 x_4 x_6 \\ \qquad -a_2 x_2^2 - a_3 x_4 u_g] \\ U_3 = \frac{1}{b_2}[k_3 \ sign(S_\theta) + \ddot{\theta}_d + \alpha_3 (\dot{\theta}_d - x_4) - a_4 x_2 x_6 \\ \qquad -a_5 x_4^2 - a_6 x_2 u_g] \\ U_4 = \frac{1}{b_3}[k_5 sign(S_\psi) + \ddot{\psi}_d + \alpha_5 (\dot{\psi}_d - x_6) - a_7 x_2 x_4 \\ \qquad -a_8 x_6^2] \end{cases} \tag{48}$$

and

$$\begin{cases} U_x = \frac{M}{U_1}(k_7 sign(S_7) + \ddot{x}_d - a_9 \hat{x}_8 - K_8 sat(e_7) - \dot{\beta}_8 + \alpha_7(\dot{x}_d - \hat{x}_8 - \beta_8)) \\ U_y = \frac{M}{U_1}(k_9 sign(S_9) + \ddot{y}_d - a_{10} \hat{x}_{10} - K_{10} sat(e_9) - \dot{\beta}_{10} + \alpha_9(\dot{y}_d - \hat{x}_{10} - \beta_{10})) \end{cases} \tag{49}$$

Fig. 3 shows the block diagram of the sliding mode observer developed in this work.

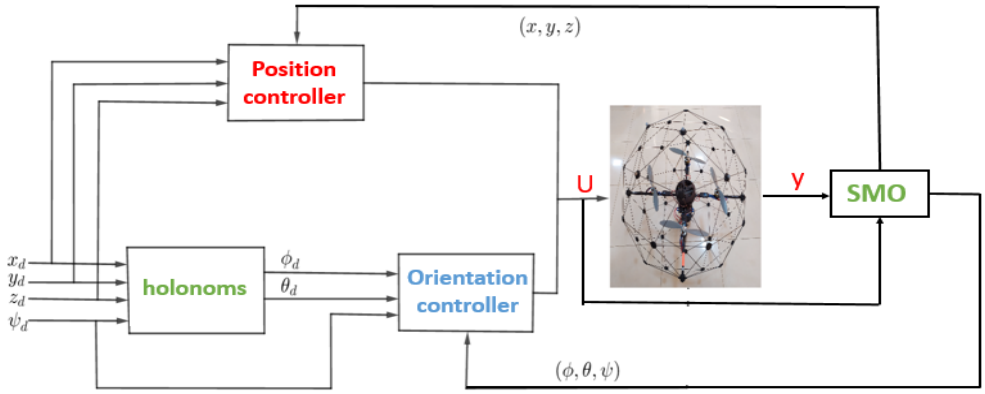

Fig. 3. Block diagram of the sliding mode observer.

The Qball 2+ control architecture is composed of three main blocks, the position control block to control the translations (x, y, z), the orientation control block to control the attitude (φ, θ, ψ) and the sliding mode observer block (see Fig. 3). The latter is used in order to replace the Flex 3 cameras when the drone is outside the working environment of the cameras. In this case, the states of the system are not measurable and the control of the drone will be lost.

4. Simulation Results

Before displayed the obtained results, the parameters of Qball 2+ are presented in Table 2. The PID and SMO observer parameters are given in Table 3, Table 4 and Table 5 respectively. Fig. 4, Fig. 5, Fig. 6, and Fig. 7 show the simulation results of the PID controller.Fig. 8, Fig. 9 and Fig. 10 show the simulation results of the SMO.

Table 2. QBall 2+ parameters.

Parameter	Definition	Value	Unit
K_t	Lift coefficient	12	N
K_d	Drag coefficient	0.4	N.m
K_v	Transformation constant	106.8	rad.s V^{-1}
M	Mass	1.79	Kg
L	Distance between the center of gravity and the center of each rotor	0.2	m
I_x	Moment of inertia of QBall 2 with respect to X axis	0.03	Kg.m^2
I_y	Moment of inertia of QBall 2 with respect to Y axis	0.03	Kg.m^2
I_Z	Moment of inertia of QBall 2 with respect to Z axis	0.04	Kg.m^2
J_{rz}	Moment of inertia of rotor with respect to Z axis	0.0018	Kg.m^2
ω	Actuator bandwith	15	rad/s
V_{max}	Maximum input voltage	12	V

4.1. Result and Discussion

Fig. 4 and Fig. 5 show that the evolution curves of the positions x, y and z follow the desired states with some errors. These latter appear when the quadrotor changes its positions. For the attitude dynamics, it's observed from Fig. 5 and Fig. 6 that, the Euler angles (ϕ, θ, ψ) follow the reference angles with less accuracy compared to the positions (x, y, z). The control signals displayed in Fig. 7 vary according to the change of their corresponding positions (see Fig. 5). Overall, the results obtained by the PID controller are acceptable.

Table 3. PID controller parameters used in simulations.

z	$K_{pz} = 0.5, K_{iz} = 0.02, K_{dz} = 0.15$	ϕ	$K_{p\phi} = 2, K_{i\phi} = 0, K_{d\phi} = 0.3$
x	$K_{px} = 0.5, K_{ix} = 0, K_{dx} = 0.4$	θ	$K_{p\theta} = 2, K_{i\theta} = 0, K_{d\theta} = 0.3$
y	$K_{py} = 0.5, K_{iy} = 0, K_{dy} = 0.4$	ψ	$K_{p\psi} = 0.45, K_{i\psi} = 0, K_{d\psi} = 0.3$

Table 4. SMO parameters used in simulations.

k_1	k_3	k_5	k_7	k_9	k_{11}	β_8	β_{10}	β_{12}	$\dot{\beta}_8$	$\dot{\beta}_{10}$	$\dot{\beta}_{12}$
5	5	4.5	9	9	15	0.3	0.35	0.9	1.4	1.2	1.3
α_1	α_3	α_5	α_7	α_9	α_{11}	K_8	K_{10}	K_{12}			
6	7	7	5	5	12	1	1.5	1.3			

Table 5. Observer gains.

Parameter	K1	K2	K3	K4	K5	K6	K7	K8	K9	K10	K11	K12
Values	15	17	10	13	12	16.5	14	15	11	13	14.5	17

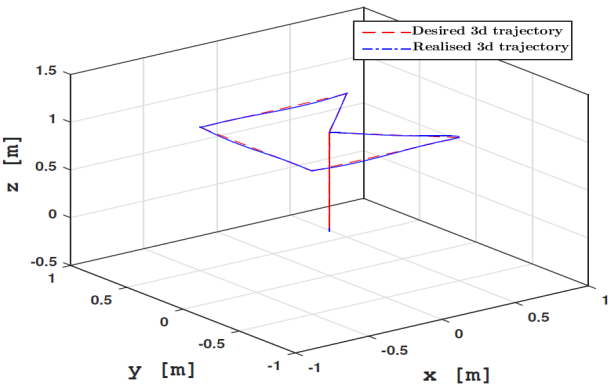

Fig. 4. Evolution of 3D trajectory for the PID controller.

Fig. 8 and Fig. 9 display the evolution of the desired trajectory, realized trajectory and the observed trajectory of the Qball 2+. It's clear that the trajectory realized by the QBall 2+ follows the reference trajectory with some tracking errors in the beginning (see Fig. 8 and Fig. 9). It can be concluded that the observed states converge rapidly towards the desired states in a finite time, whether for the positions or the Euler angles. Fig. 10 shows the evolution of the control signals. The controller U_1 starts from a maximum value and then stabilizes around a constant value. It is clear that the evolution of U_2, U_3 and U_4 depends on the evolution of the translation and the rotation of the quadrotor (see Fig. 10). The obtained results (see Fig. 8, Fig. 9 and Fig. 10), have shown that the sliding mode observer has proven its efficiency against uncertain parameters of the system.

4.2. Comparative Study

In this section, a comparative study between two control laws simulated previously (PID and SMO) will be carried out. With the aim to facilitate the comparison between the applied control laws,

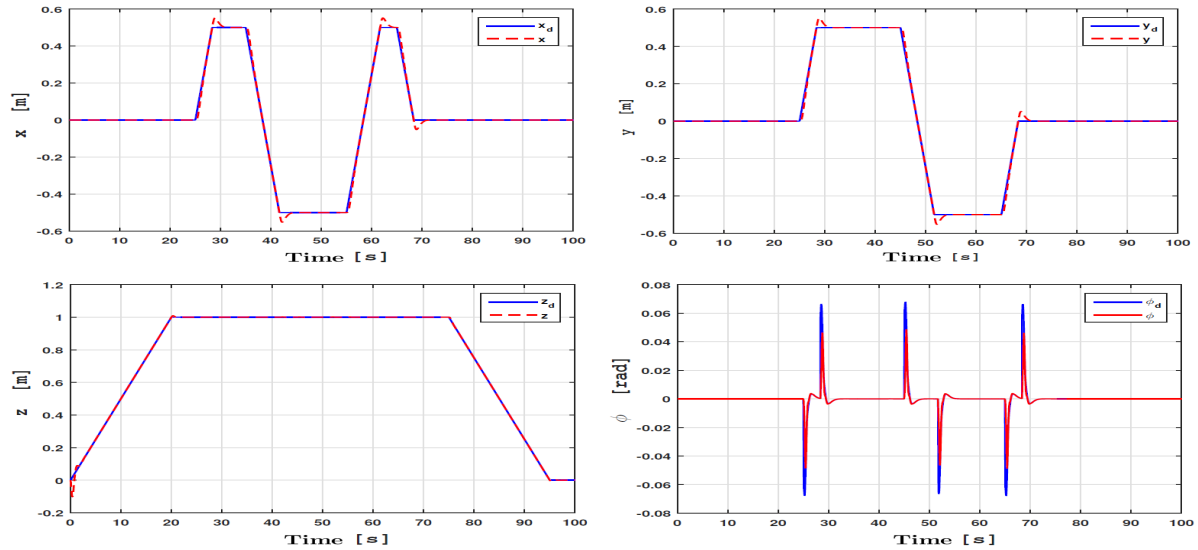

Fig. 5. Evolution of positions and roll angles for the PID controller.

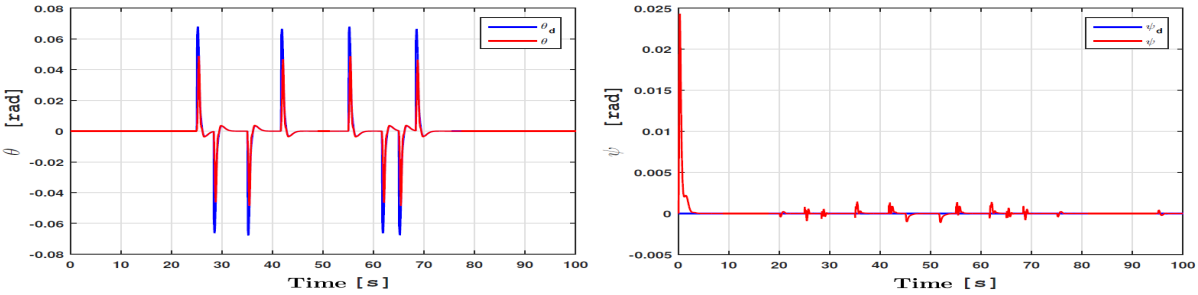

Fig. 6. Evolution of pitch and yaw angles for the PID controller.

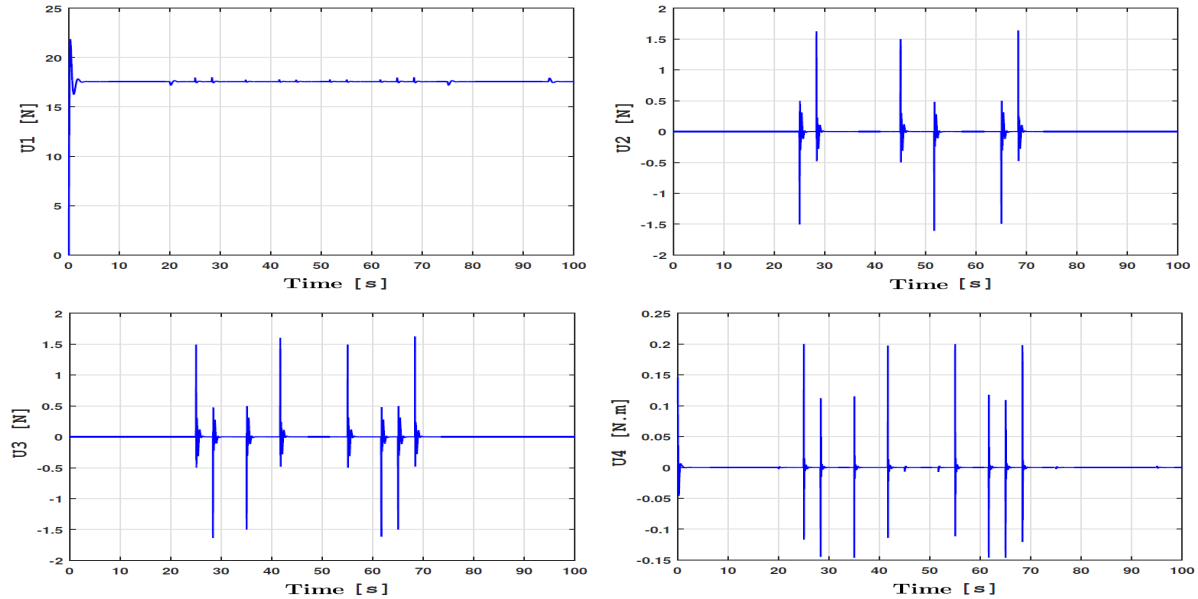

Fig. 7. Input signals for the PID controller.

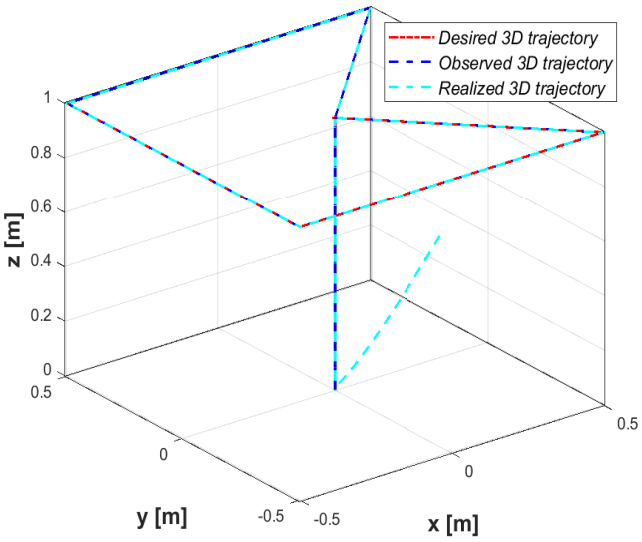

Fig. 8. Evolution of 3D trajectory for SMO.

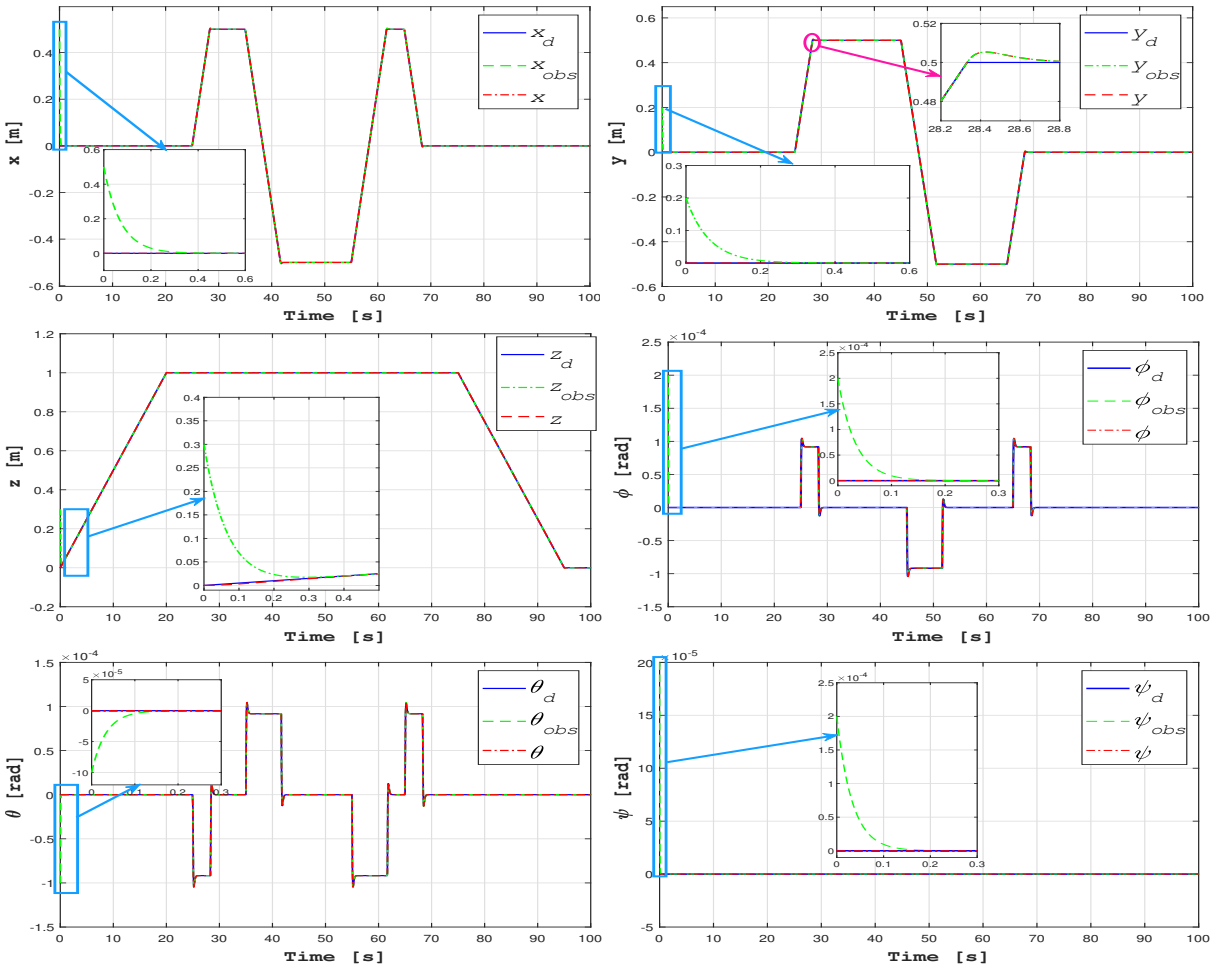

Fig. 9. Evolution of positions and Euler angles for the SMO.

two criteria will be adopted as follows:

$$J(e) = \frac{1}{k}\sum_{i=1}^{k}(e_x^2 + e_y^2 + e_z^2 + e_\theta^2 + e_\phi^2 + e_\psi^2)$$

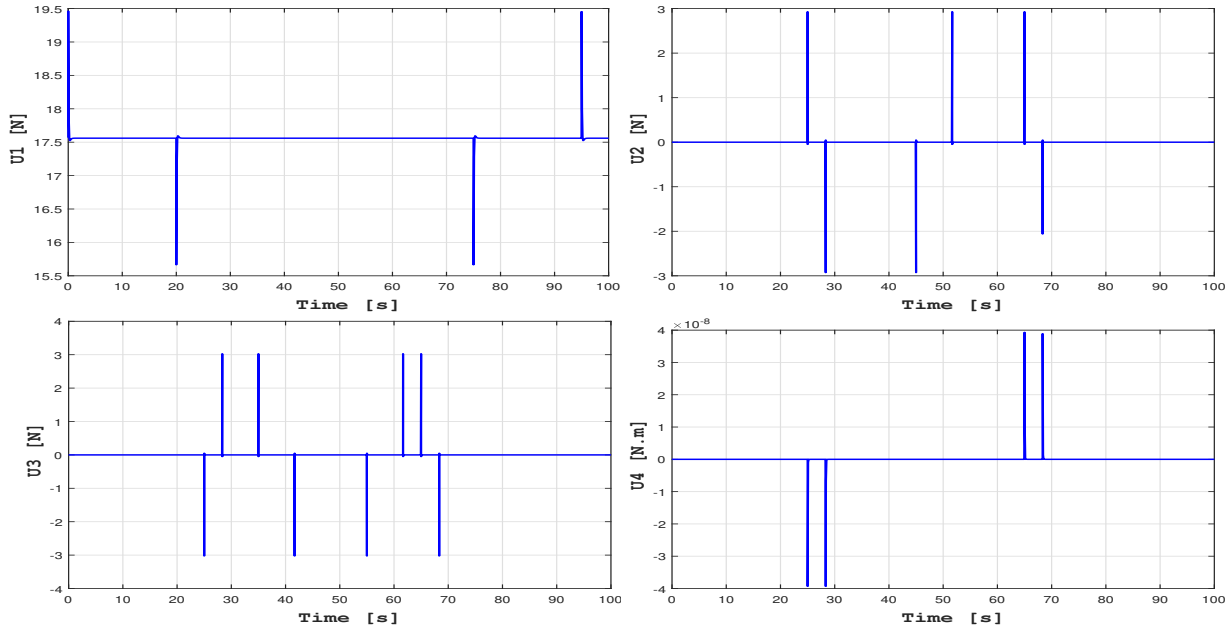

Fig. 10. Input signals for the SMO.

$$J(u) = \frac{1}{k}\sum_{i=1}^{k}(u_1^2 + u_2^2 + u_3^2 + u_\theta^2 + u_x^2 + u_y^2)$$

where $J(e)$ represents the quadratic tracking error, $J(u)$ represents the energy and k is the number of samples.

4.2.1 Results Interpretation

In this part, the energies of the control signals and their quadratic errors in a simulation time of $100s$ and a sampling step $10^{-3}s$ will be calculated. According to the criteria of the squared errors and energies (see Table 6), it can be observed that, the SMO has proven its effectiveness in terms of accuracy and consumed energy compared to the results obtained by the conventional PID. Unlike the obtained results in works [33, 34, 35, 36, 37, 38, 39, 40, 41, 42, 43, 44], where the initial conditions are zero, the SMO has presented good performance.

Table 6. Energies and quadratic errors of the controllers

	PID		SMO	
	J(e)	J(u)	J(e)	J(u)
	20.41823 10^{-6}	3.0852 10^{2}	7.280 10^{-6}	3.0836 10^{2}

5. Experimental validation

In this Section, a PID controller will be implemented in the control flight of QBall 2+ with the same parameters that we have used in simulation. Before launching the flight scenario, the different cameras "Optitrack Flex-3" must be calibrated and tested to locate the drone position as shown in Fig. 13, Fig. 14, Fig. 15 and Fig. 16.

Fig. 11. To the left, QBall 2+ equipments. To the right, QBall 2+ in flight tests.

5.1. Cameras Flex-3 calibration steps

1. Launching the motivates software to determine the limits of the field of view.
2. Checking if there are no stray objects in the field of vision.
3. Definition of the origin or center of the workplace.
4. Definition of the traceable objective by selecting reflective markers.
5. Determination of the center of the traceable objective to follow it.

Fig. 12. Optihub and cameras optitrack.

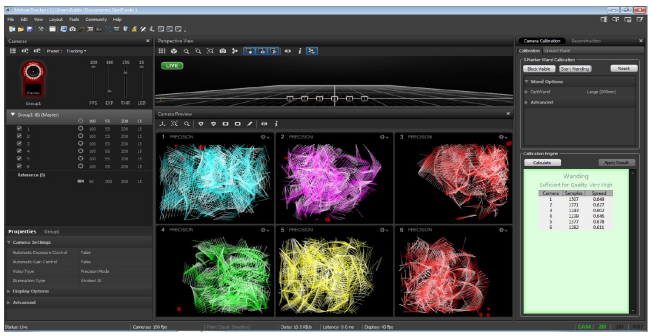

Fig. 13. Cameras Flex-3 calibration.

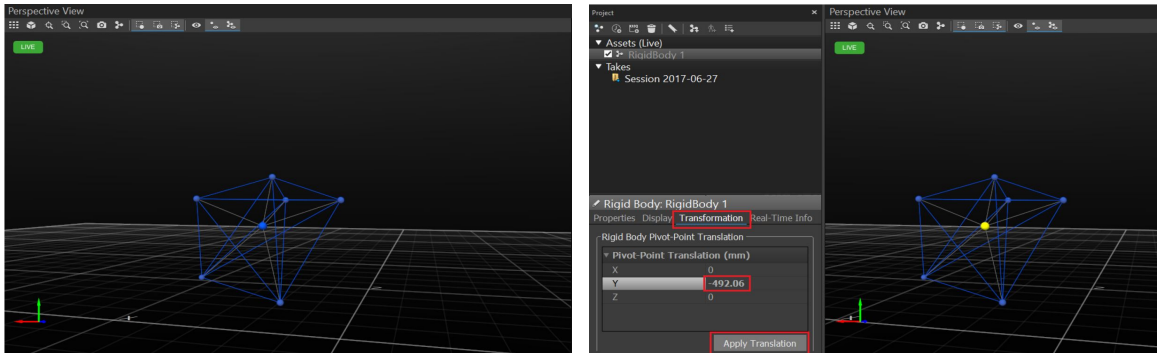

Fig. 14. Definition of the traceable objective.

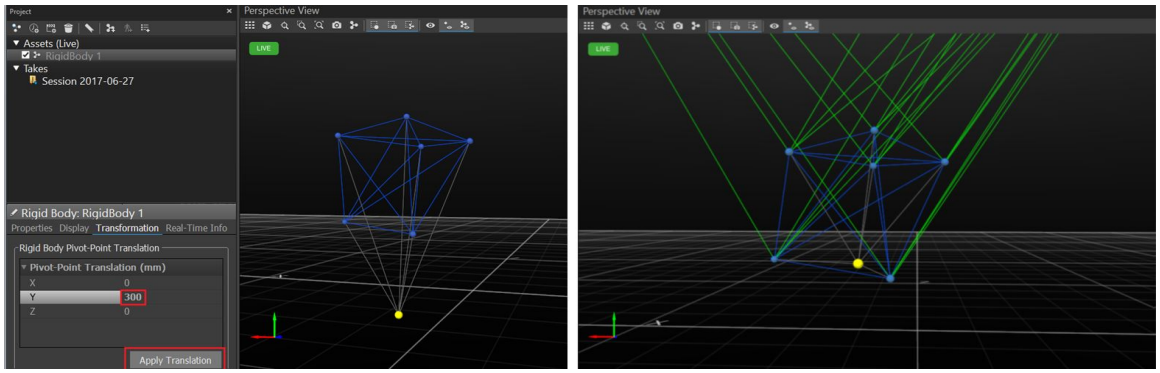

Fig. 15. Created the rigid body.

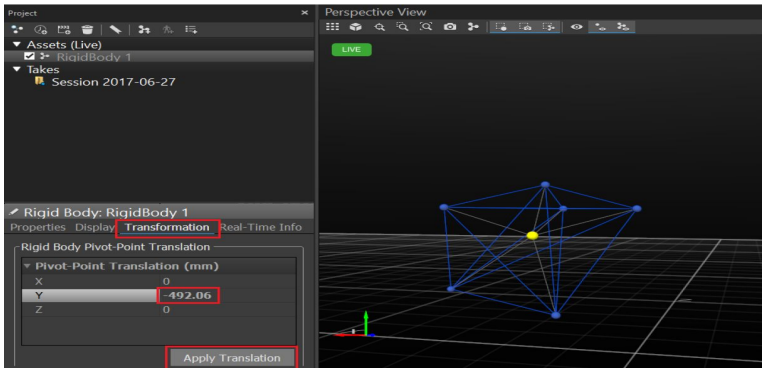

Fig. 16. Change of the geometric center of the body.

5.2. Flight Scenario

The QBall 2+ is controlled to follow the desired points in a frame of $-0.3m$ to $0.3m$. After reaching a safety height of 1 meter, the quadrotor moves in the plane (X-Y) passing through the desired points (way points) as shown in Fig. 17. The experiment results (see Fig. 17, Fig. 18, Fig. 19 and Fig. 20) have shown similarities with those obtained by simulation (see Fig. 4, Fig. 5 and Fig. 7). Effectively, the difference between the obtained results (simulation and experiment) is mainly due to the neglected parameters of the model used in simulation.

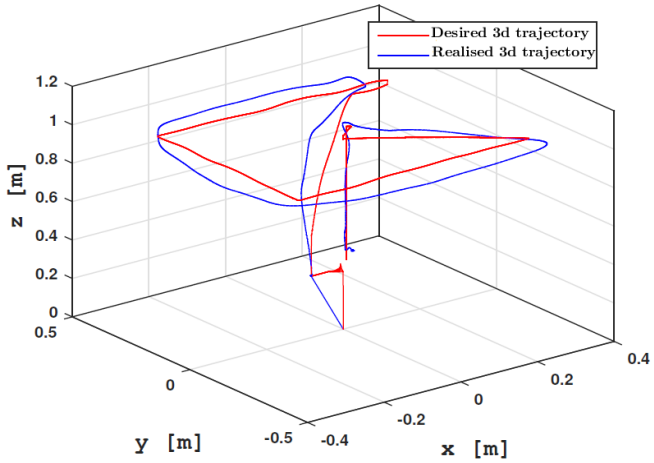

Fig. 17. Evolution of 3D trajectory for PID controller in experimental tests.

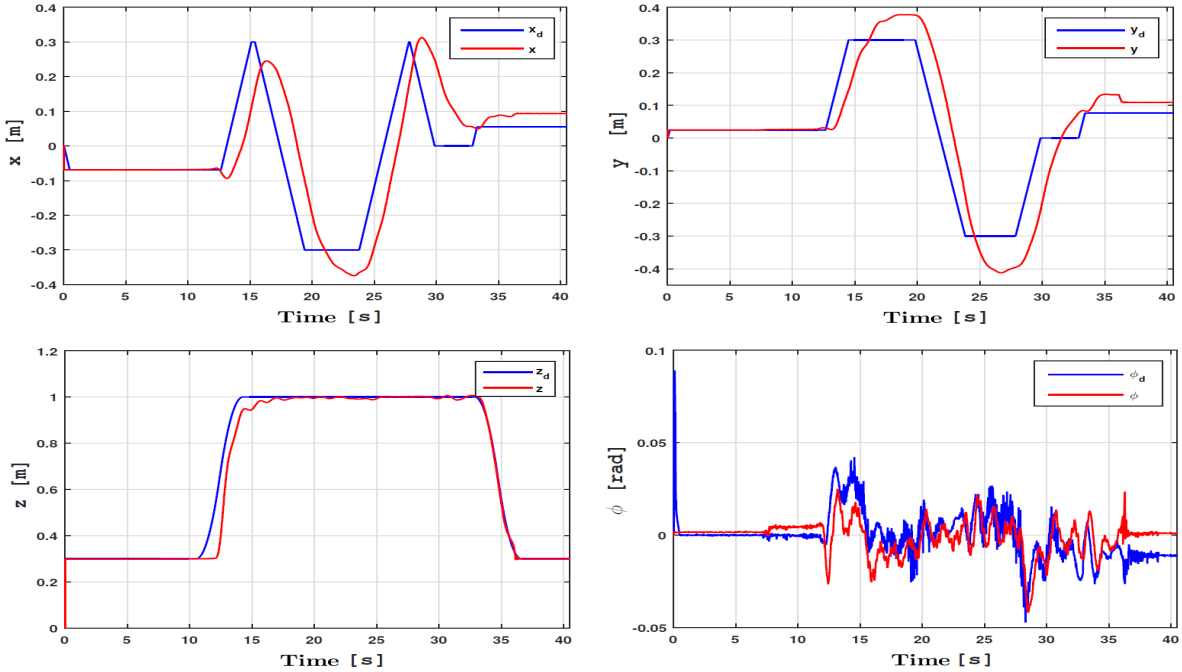

Fig. 18. Evolution of positions and roll angle in experimental tests.

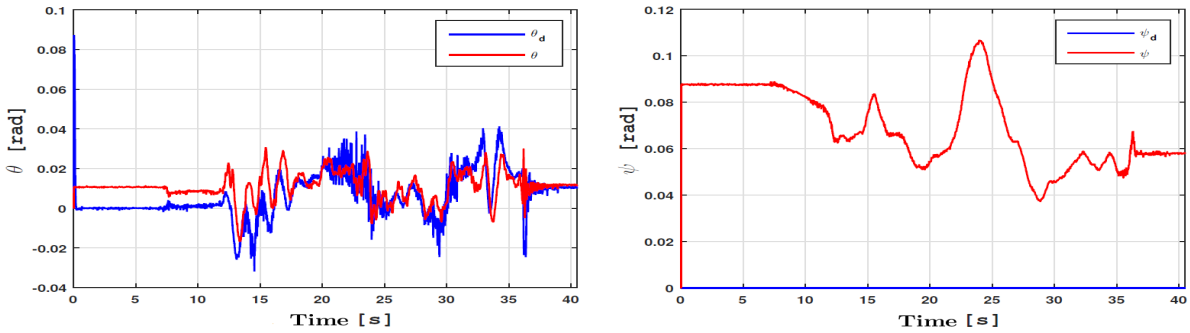

Fig. 19. Evolution of pitch and yaw angles in experimental tests.

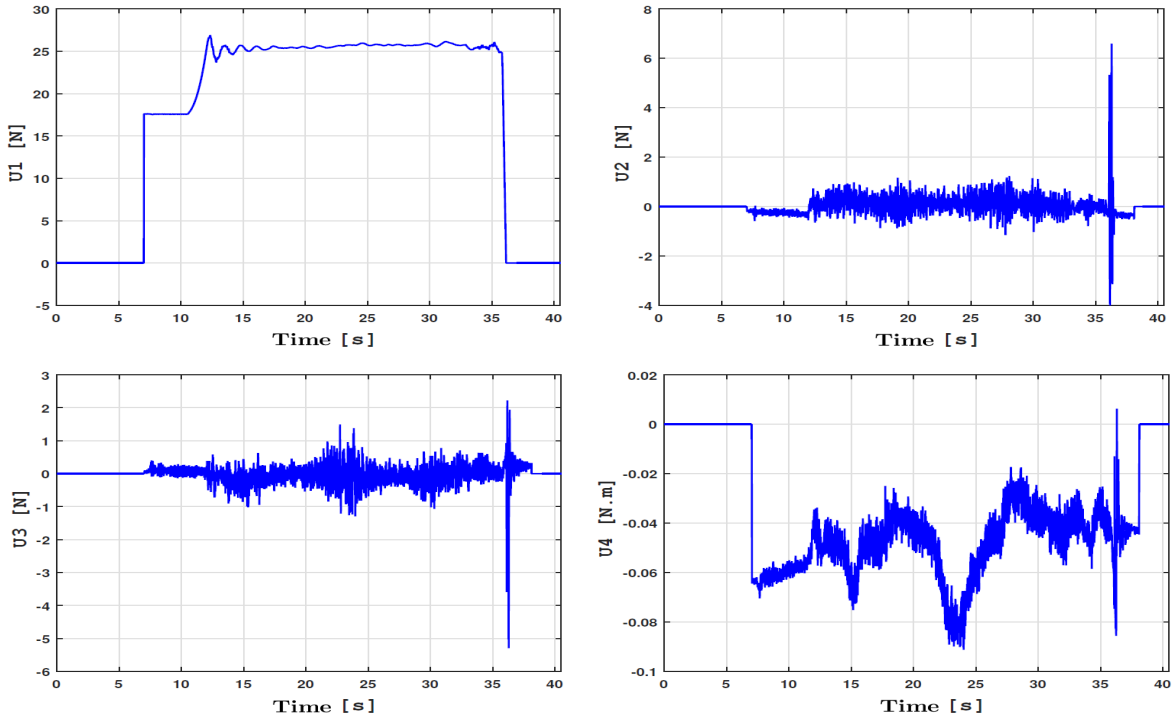

Fig. 20. Evolution of control signals in experimental tests.

6. Conclusion and Future Works

Within this article, a dynamic model of the QBall 2+ quadrotor has been developed. In addition, its linear model has been exploited to obtain the appropriate gains of the PID controller. Furthermore, to estimate the uncertain parameters of the system, a nonlinear SMC based on SMO has been developed. The latter has proven its efficiency and robustness against these parameters. Finally, to validate the obtained simulation results, the PID controller has been implemented in the flight control of the QBall 2+. The obtained results of the flight tests have shown a similitude to those obtained by simulation. In future works, the designed observer will be implemented and tested in the real system. In addition, the fault tolerant control problem will also be investigated.

Author Contribution: All authors contributed equally to the main contributor to this paper. All authors read and approved the final paper.
Funding: This research received no external funding.
Conflicts of Interest: The authors declare no conflict of interest.

References

[1] I. Moad, M. Bouzid, M. Salami, and A. Fawaz, "A Review of Quadrotor Unmanned Aerial Vehicles: Applications, Architectural Design and Control Algorithms," *Journal of Intelligent & Robotic Systems*, vol. 104, no. 2, pp. 1-33, 2022, https://doi.org/10.1007/s10846-021-01527-7.

[2] S. H. Derrouaoui, Y. Bouzid, M. Guiani, and I. Dib, "A comprehensive review on reconfigurable drones: Classification, characteristics, design and control technologies," *Unmanned Systems*, vol. 10, no. 01, pp. 3-29, 2022, https://doi.org/10.1142/S2301385022300013.

[3] S. H. Derrouaoui, Y. Bouzid, and M. Guiani, "PSO Based Optimal Gain Scheduling Backstepping Flight Controller Design for a Transformable Quadrotor," *Journal of Intelligent & Robotic Systems*, vol. 102, no. 3, pp. 1-25, 2021, https://doi.org/10.1007/s10846-021-01422-1.

[4] S. H. Derrouaoui, Y. Bouzid, and M. Guiani, "Towards a New Design with Generic Modeling and Adaptive Control of a Transformable Quadrotor," *The Aeronautical Journal*, vol. 125, no. 1294, pp. 2169–2199, 2021, https://doi.org/10.1017/aer.2021.54.

[5] F. Muñoz, N. S. Zúñiga-Peña, L. R. G. Carrillo, E. S. Espinoza, S. Salazar, and M. A. Márquez, "Adaptive Fuzzy Consensus Control Strategy for UAS-Based Load Transportation Tasks," *IEEE Transactions on Aerospace and Electronic Systems*, vol. 57, no. 6, pp. 3844-3860, 2021, https://doi.org/10.1109/TAES.2021.3082711.

[6] L. Quan, L. Han, B. Zhou, S. Shen, and F. Gao, "Survey of UAV motion planning," *IET Cyber-systems and Robotics*, vol. 1, no. 2, pp. 14-21, 2020, https://doi.org/10.1049/iet-csr.2020.0004.

[7] S. H. Derrouaoui, Y. Bouzid, and M. Guiani, "Adaptive integral backstepping control of a reconfigurable quadrotor with variable parameters' estimation," *Proceedings of the Institution of Mechanical Engineers, Part I: Journal of Systems and Control Engineering*, p. 09596518221087803, 2022, https://doi.org/10.1177%2F09596518221087803.

[8] G. Nelson, M. Asaph, and K. Mercy, "A review of quad-rotor UAVs and their motion planning," *Proceedings of the Sustainable Research and Innovation Conference*, pp. 117–121, 2022, https://sri.jkuat.ac.ke/jkuatsri/index.php/sri/article/view/81.

[9] Z. Zuo, "Trajectory tracking control design with command-filtered compensation for a quadrotor," *IET Control Theory and Application*, vol. 4, pp. 2343-2355, 2009, https://doi.org/10.1049/iet-cta.2009.0336.

[10] I. Sa and P. Corke, "Vertical infrastructure inspection using a quadcopter and shared autonomy control," *Field and Service Robotics*, vol. 92, pp. 219-232, 2014, https://doi.org/10.1007/978-3-642-40686-7_15.

[11] K. Máthé and L. Buşoniu, "Vision and control for UAVs: A survey of general methods and of inexpensive platforms for infrastructure inspection," *Sensors*, vol. 15, no. 7, pp. 14887-14916, 2015, https://doi.org/10.3390/s150714887.

[12] S. H. Derrouaoui, Y. Bouzid, and M. Guiani, "Nonlinear Robust Control of a New Reconfigurable Unmanned Aerial Vehicle," *Robotics*, vol. 10, no. 2, p. 76, 2021, https://doi.org/10.3390/robotics10020076.

[13] Quanser Innovate Educate, "Quanser Qball-2 user manual," 2017, https://www.google.com/search?q=Quanser+Innovate+Educate%2C+%E2%80%9CQuanser+Qball-2+user+manual.

[14] J. Ligthart, P. Poksawat, L. Wang, and H. Nijmeijer, "Experimentally validated model predictive control for a hexacopter," *IFAC PapersOnLine*, vol. 50, pp. 4076-4081, 2017, https://doi.org/10.1016/j.ifacol.2017.08.791

[15] R. Damen, M. Reyhanoglu, W. MacKunis, and J. R. Hervas, "Passivity-based quaternion feedback control of a hover system," *2016 16th International Conference on Control, Automation and Systems (ICCAS)*, pp. 201-206, 2016, https://doi.org/10.1109/ICCAS.2016.7832321.

[16] M. Reyhanoglu and M. Rehan, "Nonlinear dynamics and control of aerial robots," *Chapter in Aerial Robots Aerodynamics, Control, and Applications, InTech*, pp. 103-121, 2017, http://dx.doi.org/10.5772/intechopen.69641.

[17] P. Yang, Z. Zhang, H. Geng, B. Jiang, and X. Hu, "Intelligent Discrete Sliding Mode Predictive Fault-Tolerant Control Method for Multi-Delay Quad-Rotor UAV System Based on DIECOA," *Aerospace*, vol. 9, no. 4, p. 207, 2022, https://doi.org/10.3390/aerospace9040207.

[18] F. Chen, W. Lei, G. Tao, and B. Jiang, "Actuator fault estimation and reconfiguration control for the quadrotor helicopter," *International Journal of Advanced Robotic Systems*, vol. 13, no. 1, p. 33, 2016, https://doi.org/10.5772/62224.

[19] F. Pan, L. Liu, and D. Xue, "Optimal PID controller design with Kalman filter for Qball-X4 quad-rotor unmanned aerial vehicle," *Transactions of the Institute of Measurement and Control*, vol. 39, no. 12, pp. 1785–1797, 2017, https://doi.org/10.1177/0142331216656753.

[20] P. Lambert and M. Reyhanoglu, "Observer-Based Sliding Mode Control of a 6-DOF Quadrotor UAV," *IECON 2018 - 44th Annual Conference of the IEEE Industrial Electronics Society*, pp. 2379-2384, 2018, https://doi.org/10.1109/IECON.2018.8592769.

[21] M. Chen, S. Xiong, and Q. Wu, "Tracking Flight Control of Quadrotor Based on Disturbance Observer," *IEEE Transactions on Systems, Man, and Cybernetics: Systems*, vol. 51, no. 3, pp. 1414-1423, 2021, https://doi.org/10.1109/TSMC.2019.2896891.

[22] L. M. Elamine, K. Z. Meguenni, M. Youssouf, and L. Mustapha, " Nonlinear observer, and PI-backstepping controller for unmanned aerial vehicle type quadrotor," *International Journal of Industrial Electronics and Drives*, vol. 1, no. 4, 2014, https://doi.org/10.1504/IJIED.2014.066214.

[23] J. Moreno-Valenzuela, R. Pérez-Alcocer, M. Guerrero-Medina, and A. Dzul, "Nonlinear PID-Type Controller for Quadrotor Trajectory Tracking," *IEEE/ASME Transactions on Mechatronics*, vol. 23, no. 5, pp. 2436-2447, 2018, https://doi.org/10.1109/TMECH.2018.2855161.

[24] P. Yang, R. Guo, X. Pan, and T. Li, "Study on the sliding mode fault tolerant predictive control based on multi agent particle swarm optimization," *Int. J. Control Autom. Syst.*, vol. 15, pp. 2034–2042, 2017, https://doi.org/10.1007/s12555-016-0040-8

[25] R. Pérez-Alcocer and J. Moreno-Valenzuela, "A novel Lyapunov-based trajectory tracking controller for a quadrotor: Experimental analysis by using two motion tasks," *Mechatronics*, vol. 61, pp. 58–68, 2019, https://doi.org/10.1016/j.mechatronics.2019.05.006.

[26] Y. A. Younes, H. Noura, A. Rabhi, and A. E. Hajjaji, "Actuator Fault-Diagnosis and Fault-Tolerant-Control using intelligent-Output-Estimator Applied on Quadrotor UAV," *2019 International Conference on Unmanned Aircraft Systems (ICUAS)*, pp. 413-420, 2019, https://doi.org/10.1109/ICUAS.2019.8798232.

[27] O. Kose and T. Oktay, "Dynamic Modeling and Simulation of Quadrotor for Different Flight Conditions," *European Journal of Science and Technology*, vol. 15, pp. 132–142, 2019, https://doi.org/10.31590/ejosat.507222.

[28] B. Wang, X. Yu, L. Mu, and Y. Zhang, "A dual adaptive fault-tolerant control for a quadrotor helicopter against actuator faults and model uncertainties without overestimation," *Aerospace Science and Technology*, p. 105744, 2020, https://doi.org/10.1016/j.ast.2020.105744.

[29] K. Eliker, H. Bouadi, and M. Haddad, "Flight planning and guidance features for an uav flight management computer," *2016 IEEE 21st International Conference on Emerging Technologies and Factory Automation (ETFA)*, pp. 1–6, 2016, https://doi.org/10.1109/ETFA.2016.7733735.

[30] S. Ullah, A. Mehmood, Q. Khan, S. Rehman, and J. Iqbal, "Robust Integral Sliding Mode Control Design for Stability Enhancement of Under-actuated Quadcopter," *Int. J. Control Autom. Syst.*, vol. 18, pp. 1671–1678, 2020, https://doi.org/10.1007/s12555-019-0302-3.

[31] M. Chen, S. Xiong, and Q.Wu, "Tracking flight control of quadrotor based on disturbance observer," *IEEE Transactions on Systems, Man, and Cybernetics: Systems*, vol. 51, no. 3, pp. 1414-1432, 2021, https://doi.org/10.1109/TSMC.2019.2896891

[32] S. John, "Artificial Intelligent-Based Feedforward Optimized PID Wheel Slip Controller," *2013 AFRICON*, pp. 1-6, 2013, https://doi.org/10.1109/AFRCON.2013.6757683.

[33] Y. Al Younes, H. Noura, M. Muflehi, A. Rabhi and A. El Hajjaji, "Model-free observer for state estimation applied to a quadrotor," *2015 International Conference on Unmanned Aircraft Systems (ICUAS)*, pp. 1378-1384, 2015, https://doi.org/10.1109/ICUAS.2015.7152433.

[34] M. H. Amoozgar, A. Chamseddine, and Y. Zhang, "Experimental Test of a Two-Stage Kalman Filter for Actuator Fault Detection and Diagnosis of an Unmanned Quadrotor Helicopter," *J Intell Robot Syst*, vol. 70, pp. 107–117, 2013, https://doi.org/10.1007/s10846-012-9757-7.

[35] L. Chen, Z. Liu, H. Gao, and G. Wang, "Robust adaptive recursive sliding mode attitude control for a quadrotor with unknown disturbances," *ISA transactions*, vol. 122, pp. 114–125, 2022, https://doi.org/10.1016/j.isatra.2021.04.046.

[36] A. Noordin, M. A. M. Basri, Z. Mohamed, and I. M. Lazim, "Adaptive PID controller using sliding mode control approaches for quadrotor UAV attitude and position stabilization," *Arabian Journal for Science and Engineering*, vol. 46, pp. 963-981, 2021, https://doi.org/10.1007/s13369-020-04742-w.

[37] Y. Bouzid, S. H. Derrouaoui, and M. Guiatni, "PID Gain Scheduling for 3D Trajectory Tracking of a Quadrotor with Rotating and Extendable Arms," *2021 International Conference on Recent Advances in Mathematics and Informatics (ICRAMI)*, pp. 1-4, 2021, https://doi.org/10.1109/ICRAMI52622.2021.9585973.

[38] N. Fethalla, M. Saad, H. Michalska, and J. Ghommam, "Robust observer-based dynamic sliding mode controller for a quadrotor UAV," *IEEE access*, vol. 6, pp. 45846-45859, 2018, https://doi.org/10.1109/ACCESS.2018.2866208.

[39] Z. Zhao, D. Cao, J. Yang, and H. Wang, "High-order sliding mode observer-based trajectory tracking control for a quadrotor UAV with uncertain dynamics," *Nonlinear Dynamics*, vol. 102, no. 4, pp. 2583-2596, 2020, https://doi.org/10.1007/s11071-020-06050-2.

[40] W. Cai, J. She, M. Wu, and Y. Ohyama, "Disturbance suppression for quadrotor UAV using sliding-mode-observer-based equivalent-input-disturbance approach," *ISA transactions*, vol. 92, pp. 286–297, 2019, https://doi.org/10.1016/j.isatra.2019.02.028.

[41] H. Castañeda, J. Rodriguez, and J. L. Gordillo, "Continuous and smooth differentiator based on adaptive sliding mode control for a quad-rotor MAV," *Asian Journal of Control*, vol. 23, pp. 661-672, 2021, https://doi.org/10.1002/asjc.2249.

[42] Y. Rong, R. Jiao, S. Kang, and W. Chou, "Sigmoid super-twisting extended state observer and sliding mode controller for quadrotor uav attitude system with unknown disturbance," *2019 IEEE International Conference on Robotics and Biomimetics (ROBIO)*, pp. 2647-2653, 2019, https://doi.org/10.1109/ROBIO49542.2019.8961654.

[43] S. H. Derrouaoui, Y. Bouzid, M. Guiani, K. Halfaoui, I. Dib and M. Moudjari, "Backstepping Controller Applied to a Foldable Quadrotor for 3D Trajectory Tracking," *ICINCO*, pp. 537-544, 2020, https://www.scitepress.org/Papers/2020/98902/98902.pdf.

[44] S. H. Derrouaoui, Y. Bouzid, M. Guiani and A. Belmouhoub, "Trajectory Tracking of a Reconfigurable Multirotor Using Optimal Robust Sliding Mode Controller," *University of Eloued*, 2022, http://dspace.univ-eloued.dz/handle/123456789/10842.